Vacuum 242 (2025) 114714

Contents lists available at ScienceDirect

Vacuum

journal homepage: www.elsevier.com/locate/vacuum

Linear Al-composition dependence of strain-free bandgap in $Al_xGa_{1-x}N$ ($0 \leq x < 0.2$) via optical spectroscopy and theoretical calculation

Shaosheng Fan [a,b], Masao Ikeda [b,c,d,*], Baoping Zhang [a,e,**], Siyi Huang [c,d], Yang Mei [a], Jianping Liu [c,d], Zongliang Liu [b], Ke Xu [b,c]

[a] Laboratory of Micro/Nano-Optoelectronics, School of Electronic Science and Engineering, Xiamen University, Xiamen, 361005, People's Republic of China
[b] Jiangsu Institute of Advanced Semiconductors, Suzhou, Jiangsu, 215125, People's Republic of China
[c] Suzhou Institute of Nano-Tech and Nano-Bionics, Chinese Academy of Sciences (CAS), Suzhou, 215123, People's Republic of China
[d] Key Laboratory of Nanodevices and Applications, Suzhou Institute of Nano-Tech and Nano-Bionics, Chinese Academy of Sciences (CAS), Suzhou, 215123, People's Republic of China
[e] Institute of Nanoscience and Applications & College of Semiconductors, Southern University of Science and Technology, Shenzhen, 518055, People's Republic of China

ARTICLE INFO

Handling Editor: Prof. L.G. Hultman

Keywords:
AlGaN
Critical thickness
In-plane biaxial strain
Bowing parameter
Photoluminescence
Reflectance

ABSTRACT

This study presents the strain-free bandgap energy derived from the pseudomorphic $Al_xGa_{1-x}N$ layer, obtained through theoretical calculations and experiments. The $Al_xGa_{1-x}N$ films with various Al compositions ($0 \leq x < 0.2$) were coherently grown on GaN/sapphire templates by metal-organic chemical vapor deposition, keeping their thicknesses smaller than their critical thicknesses. The *c*-lattice constants of GaN layers onto which the $Al_xGa_{1-x}N$ layers were coherently grown were calculated considering the strain effects both from sapphire substrate and $Al_xGa_{1-x}N$ epilayer, and confirmed by measuring absolute *c*-lattice constants using two different diffraction planes (0002) and (0004) by XRD. The strain-induced shift in the $Al_xGa_{1-x}N$ bandgap energy due to the difference in thermal expansion coefficients between sapphire and nitrides and in-plane biaxial strain caused by a lattice-mismatch with GaN was calculated based on the band parameters given in the literature. The excitonic transition energy for fully-strained $Al_xGa_{1-x}N$ films was obtained based on the temperature-dependent photoluminescence, and confirmed also by observing exciton-related features in reflectance measurements at room temperature. By accounting for the bandgap shift induced by strain and the exciton binding energies, the Al-composition dependence of the strain-free bandgap energy was determined, yielding no bowing parameter.

1. Introduction

AlGaN alloy layers with low Al composition play important roles in nitrides-based devices as cladding layers [1] and an electron blocking layer in nitride-based laser diodes and light emitting diodes [2] in the violet to green spectral range, and as a barrier layer in high electron mobility transistors [3]. It can also be used as the main light-emitting layer [4,5] in applications in the ultraviolet spectrum range.

Among the most fundamental properties of $Al_xGa_{1-x}N$, the change of bandgap energy, E_g, as a function of Al-content, x, was investigated actively around year 2000. Lee et al. [6] summarized and concluded that E_g of $Al_xGa_{1-x}N$ grown on high-quality GaN/sapphire template changes with a bowing parameter of 0.6–0.7 eV, by properly taking into account the strain effects, and making sure the consistency with many other reports. They also pointed out that the AlGaN layers on sapphire substrate typically exhibit stronger bowing due to the sub-gap states originating from the materials-quality issues.

However, some questions still remain. The first issue is regarding the endpoint E_g of AlN, for which all these early reports assumed the old value of 6.2 eV at room temperature, which was evaluated from somehow defective AlN directly grown on sapphire at 1100 °C by vapor phase reaction between aluminum chlorides with ammonia [7]. But lately, E_g for a higher quality AlN layer homoepitaxially grown on bulk AlN substrates was reported to be 6.094 eV [8] and 6.095 eV [9] at ~10 K. Both of these were determined by adding the exciton binding energy of 52 ± 1 meV to the measured lowest free-exciton transition energy of

* Corresponding author. Jiangsu Institute of Advanced Semiconductors, Suzhou, Jiangsu, 215125, People's Republic of China.
** Corresponding author. Laboratory of Micro/Nano-Optoelectronics, School of Electronic Science and Engineering, Xiamen University, Xiamen, 361005, People's Republic of China.
E-mail addresses: mikeda2013@sinano.ac.cn (M. Ikeda), bzhang@xmu.edu.cn (B. Zhang).

https://doi.org/10.1016/j.vacuum.2025.114714
Received 10 March 2025; Received in revised form 31 August 2025; Accepted 2 September 2025
Available online 3 September 2025

6.042 ± 0.002 eV. Therefore, if considering the temperature shrinkage in E_g of 85 ± 5 meV, which is the average value between the experimental ~80 meV [10] and calculated 90 meV [11] using the Varshni formula, the room temperature E_g of AlN should be 6.01 ± 0.01 eV, in agreement with the 6.012 eV [12] reported by Feneberg et al. The revised E_g value of AlN might lead to a smaller bowing parameter to half of Lee's value. The second issue is related to the evaluation methods of E_g. The photoluminescence (PL) and reflectance measurements at room temperature are commonly used to evaluate E_g, the PL peak and Reflectance signals generally correspond to the free excitonic transition energies, which are lower by the exciton binding energies than the bandgap energy (band-to-band), because the exciton binding energies in AlGaN become larger than k_BT at room temperature. Nevertheless, the early works simply approximated E_g with the energies of these signals, ignoring the exciton binding energies. In addition, the A- and B-excitons are not resolved at room temperature due to the thermal broadening, thus the signals must be analyzed taking into account both contributions from A- and B-excitons. Since the exciton binding energy in $Al_xGa_{1-x}N$ increases with x because of the increasing reduced mass, the Lee's value of the bowing parameter would be further reduced when the change in binding energy with x is properly taken into account. The third is regarding the sample structure, i.e., the thickness of $Al_xGa_{1-x}N$. When the $Al_xGa_{1-x}N$ is heterogeneously grown on GaN, cracks or misfit dislocations will be formed if the $Al_xGa_{1-x}N$ thickness exceeds the critical value, referred as critical layer thickness. In this case, the strain state of $Al_xGa_{1-x}N$ varies spatially depending on the distance from the crack or dislocation [13]. This spatial non-uniformity of strain state results in the spatial non-uniformity of materials properties, which would cause some measurement errors in determining E_g and x. And it is widely known that accurately assessing the degree of strain relaxation is a complex and time-consuming task, and the errors in strain evaluation can affect subsequent assessments of bandgap shifts due to strain. Therefore, using fully strained $Al_xGa_{1-x}N$ films not only improves the experimental accuracy but also simplifies the measurement characterization process. It is desired to use the $Al_xGa_{1-x}N$ samples thinner than the critical thickness. However, in the early works, some experiments [6,14] were performed including AlGaN layers apparently thicker than the critical thickness. Judging from the above three points, it is considered to be quite necessary to revisit the old topic of AlGaN bandgap dependence on Al composition.

In this study, all the $Al_xGa_{1-x}N$ samples used were chosen to be fully strained layers, thinner than the critical thickness, without surface cracks. High-resolution TEM and XPS analyses confirm that the AlGaN films possess high crystalline quality, coherent epitaxial growth, and favorable bonding characteristics. The strain state of $Al_xGa_{1-x}N$ was determined by a model calculation, and confirmed by measuring the GaN strain experimentally using the two-diffraction-planes XRD method [15]. The strain state of AlGaN was then determined assuming perfect in-plane lattice matching to GaN underlayers. The biaxial-strain shift of E_g was calculated theoretically [16] based on the band parameters, such as valence band deformation potential constants, crystal field and spin-orbit splitting, and hydrostatic deformation potential constants together with stiffness constants given in the literature [11]. The excitonic transition energies for fully-strain $Al_xGa_{1-x}N$ films were measured by temperature-dependent PL (TDPL) and reflectance at room temperature. The PL peak energies were in good agreement with the central spectral lineshape observed in the reflectance at room temperature. The strain-free E_g was determined based on the excitonic transition energies with taking into account both the strain-induced shift and the exciton binding energy. The resulting strain-free E_g changed linearly with x, without any bowing.

2. Experiment

The $Al_xGa_{1-x}N$ epilayers with various Al compositions ($0 \leq x < 0.2$) were coherently grown on c-plane GaN-on-sapphire templates (3 μm high-temperature GaN on ~30 nm thick low-temperature GaN buffer deposited on 430 μm-thick sapphires) in a horizontal flow TNSC MOCVD reactor. In addition, some extra coherent $Al_xGa_{1-x}N$ layers were grown on the free-standing GaN (FS-GaN) substrate for comparison. The $Al_xGa_{1-x}N$ layers had decreasing thicknesses with increasing alloy composition so that their thicknesses could be kept slightly smaller than the critical thickness at the corresponding compositions. The precursors used were trimethylgallium (TMG), trimethylaluminum (TMA), and ammonia (NH_3) for the Al, Ga, and N elements, respectively. The $Al_xGa_{1-x}N$ films were grown at a temperature of 960 °C under atmospheric pressure using H_2 carrier gas. The flow rate of the TMG varied from 22 to 100 sccm, corresponding from 31.0 to 141.1 μmol/min. Together with a constant flow rate of 13.5 μmol/min for TMA, the Al composition ranging from 0 to 20 % was obtained. Then the total flow rate was fixed at 72 slm. On the GaN/Sapphire template or FS-GaN substrate, all the samples were initiated by growing a ~1 μm GaN layer. For GaN sample ($x = 0$), a ~100 nm-thick $In_{0.08}Ga_{0.92}N$ was inserted between the top GaN and GaN template to exclude the influence of the low-quality GaN near the GaN/sapphire interface in the optical measurements. The $Al_xGa_{1-x}N$ thickness was basically determined by the growth rate. Calibration was also performed by using AlGaN/GaN superlattice (SL) underneath the $Al_xGa_{1-x}N$, where the period determined by the satellite peaks of SL in the XRD could be used to calibrate the thickness of the top AlGaN (Al composition of the thin AlGaN in the SL was set identical to the thick top AlGaN). The thickness of AlGaN was also checked by the interference fringes observed in the ω–2θ XRD pattern (Fig. S1 as shown in supplementary material).

Detailed microstructural observations were recorded using a high-resolution Transmission Electron Microscope (HR-TEM) of Thermo Scientific (FEI) Themis Z operating at an accelerating voltage of 300 kV and equipped with spherical aberration system. The TEM observations were taken in high-angle annular dark field (HAADF) modes and were complemented with detailed chemical composition analysis using energy dispersive X-ray spectroscopy (EDX). The passivation carbon layer was sputtered onto the sample surface to protect the sample, and then focused ion beam milling was used for the preparation of the lamella. All X-ray photoelectron spectroscopy (XPS) measurements are performed on the Thermo Fisher Scientific ESCALAB Xi + system with the base pressure of 7.5×10^{-11} Torr during spectra acquisition. Monochromatic Al Kα radiation (1486.6 eV) was employed as the X-ray excitation source, and all spectra were collected at an angle of 54° relative to the surface normal. The XPS analysis area is approximately ϕ = 500 μm. A low-energy Ar^+ ion gun (1 kV, 40° from the surface normal) was used before the XPS analysis of the samples to avoid potential ion-induced damage and remove the surface oxide thin layer. An electron–ion charge compensation system was applied to mitigate surface charging effects during the experiments. When the charge compensation system was employed, the partial pressure in the analytical chamber was maintained at 1.5×10^{-7} Torr. Since removal from the MOCVD chamber, the AlGaN samples have been stored in sealed polypropylene wafer boxes wrapped in non-woven wipers to preserve the original surface condition [17].

The optical-reflectance spectra of $Al_xGa_{1-x}N$ were taken at an incident angle of 8° with 1 × 5 mm^2 slit at room temperature with a wavelength-interval of 0.5 nm, using an Ultraviolet–Visible–Near infrared (UV–VIS–NIR) spectrometer (LAMBDA 750). Deuterium or a Tungsten lamp was used as the light source. The exciton features were not always clear depending on the phase of interference. In this case, a proper position on the wafer exhibiting clear exciton features was looked for, since the thickness and Al composition change slightly across the wafer, changing the phase of interference, and at this same position, the XRD and PL measurements were performed. The XRD measurements were performed using a Bruker D8 diffractometer, and the CuKα1 line (1.54056 Å) was selected using a 2-bounce Ge (220) monochromator. The Al composition of the AlGaN layer was measured by a $2\theta - \omega$ scan of (0002) in the triple-axis mode. For the temperature-dependent PL

measurements, the sample was mounted in a helium closed-circuit cryostat and the temperature was controlled from 3.3 to 300 K. The PL signal from the sample was dispersed by a Princeton Instruments ACTON Spectrapro-3000i monochromator with a 1200 grooves/mm grating and detected by a thermoelectrically cooled Synapse CCD detector. Depending on the Al composition, a 325 nm He-Cd laser or 278 nm laser with 5 ns pulse duration and 20 Hz repeat frequency was used as the excitation source. The surface of the samples was observed by a Nomarski interference optical microscope to make sure that there were no cracks on the surface.

3. Results and discussion

3.1. Crystalline quality of AlGaN

The thickness and microstructure of the AlGaN film were characterized using TEM. Fig. 1(a) provides a cross-sectional TEM image of the AlGaN film, revealing a thickness of 252.4 nm, consistent with the XRD results shown in Fig. 3. The uniform growth of the AlGaN and the sharp interface between AlGaN and GaN/sapphire substrate are shown in the TEM image, demonstrating good crystalline quality. To gain deeper insight into the growth of the AlGaN film, high-resolution TEM images were taken in the area near the AlGaN/GaN interface [highlighted by the green box in Fig. 1(a)]. The HR-TEM images of Fig. 1(b, c) show the excellent stacking sequence along the growth direction and no misfit dislocations in layer-by-layer, indicating the pseudomorphic growth of AlGaN on GaN/sapphire substrate. Furthermore, the EDX mapping of Fig. 1(d) shows that the three constituent elements of the AlGaN film, along with the C and O, are uniformly distributed throughout the entire film up to the surface (the increase of C content on the surface was due to the C passivation adopted in the measurement). The trace amounts of C (~4.46 at.%) and O (~3.49 at.%) impurities are likely introduced from metalorganic precursors. The low impurity content further proves the excellent crystalline quality of AlGaN films. It should be noted that the EDX mapping of oxygen reveals the presence of a thin oxygen-rich layer at the surface of the AlGaN films, which is most likely attributed to surface oxidation contamination upon air exposure.

Next, the detailed chemical states of the AlGaN film were analyzed through XPS measurements. All core levels spectra deconvolution and quantification are performed using a self-consistent peak model [18,19]. Using the C 1s peak (typically assigned at 284.0–285.2 eV) as a reference to calibrate all the core-level spectra is inherently unreliable due to the fact that the binding energy of the C 1s peak from adventitious carbon measured relative to the Fermi edge, can vary by as much as 1.44 eV [20,21]. Later, G. Greczynski and L. Hultman found that the C 1s peak actually aligns to the vacuum level, indicating that its binding energy is steered by the sample's work function. Specifically, the sum of the C 1s binding energy and the work function is constant at 289.50 ± 0.15 eV [22,23]. Accordingly, we first determined the secondary electron cutoff (SECO) of the sample to be 16.86 eV from UPS measurements (Fig. S2 as shown in the supplementary material). Using the photon energy of the He I excitation source (21.22 eV), the sample work function was calculated as $\phi_{SA} = 4.36$ eV. As a result, the corrected position of the C 1s peak was set to 289.5 eV − ϕ_{SA} = 285.14 eV.

Fig. 2(a) shows the XPS survey spectrum of the AlGaN film, revealing the presence of Al, Ga, and N elements, with their respective core level spectra as shown in Fig. 2(b, c, d), respectively. The Al 2p core level spectrum has been deconvoluted into two distinct components, located at 74.1 eV and 73.5 eV, which correspond to Al-O and Al-N bonds, respectively. The photoelectron spectrum of Ga 3d is resolved into two main subpeaks at 19.7 eV and 18.6 eV, corresponding to Ga-N and Ga-Ga bonds. The spectrum of N 1s consists of N–Al (397.6 eV), N–Ga (397.0 eV), and two Ga LMM Auger electrons [24,25] at the lower energy side. The findings are consistent with prior research confirming the synthesis of AlGaN films [26]. The presence of Al-O and unobserved Ga-O indicates that the unsatisfied bonds on Al have a higher affinity for O atoms compared to those on Ga [27]. The synthesis fraction of Ga-Ga bonding is attributed to the elevated concentration of reactive Ga atoms reaching the growth site at this temperature compared to reactive N atoms. The Al mole fractions of 10.0 % in the $Al_xGa_{1-x}N$ films were determined from the area ratio of the Al-N and Ga-N peaks (e.g., Al-N/(Al-N + Ga-N) in N 1s core spectra and were consistent with XRD

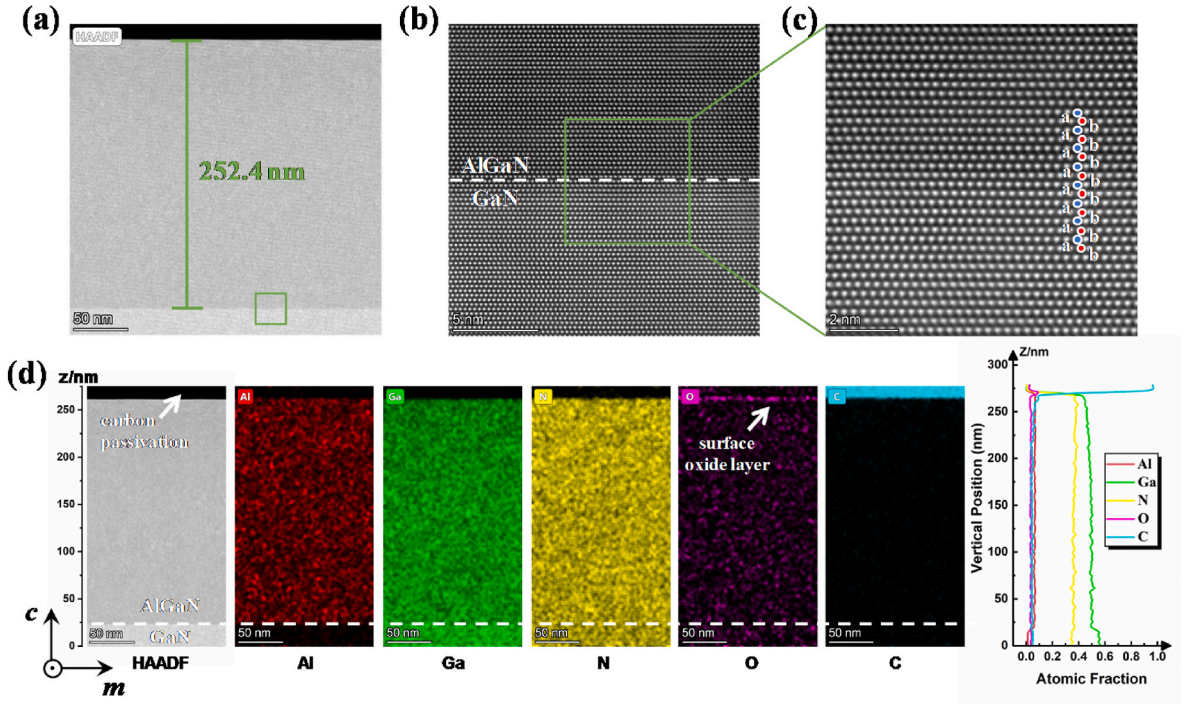

Fig. 1. (a) The HAADF images in the projection of the crystallographic a-axis for the $Al_{0.101}Ga_{0.899}N$ film. (b, c) The high-resolution TEM images identify the atomic stacking sequence. (d) EDX mappings of Al, Ga, N, O, and C.

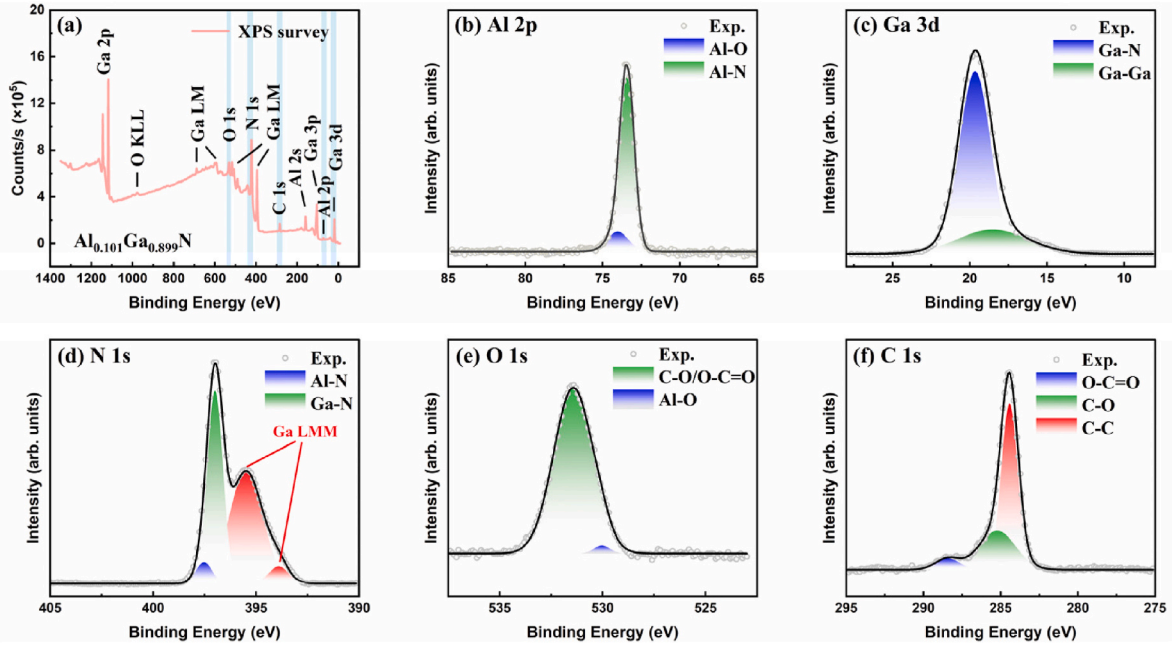

Fig. 2. (a) XPS survey spectrum of $Al_{0.101}Ga_{0.899}N$ film; (b), (c), (d), (e), and (f) Al 2p, Ga 3d, N 1s, O 1s, and C 1s core level spectra, respectively.

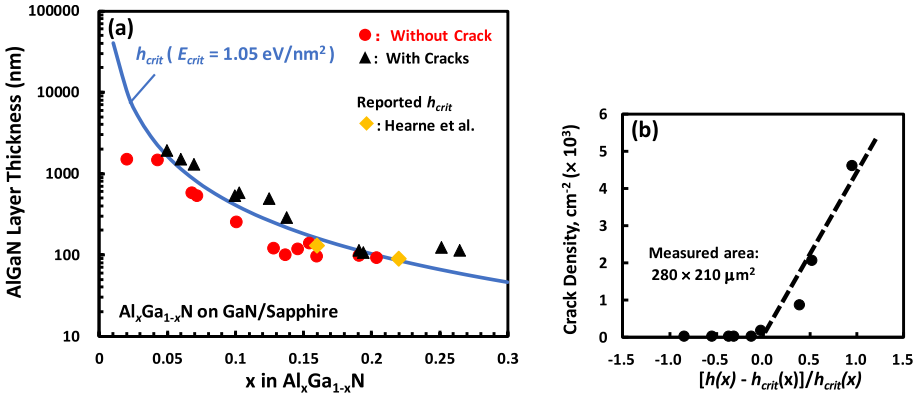

Fig. 3. (a) The calculated critical layer thickness versus Al composition for $Al_xGa_{1-x}N$ films on GaN/sapphire template (blue solid curve). Black triangles and red circles represent the thickness of samples with and without surface cracks, respectively, as observed by an interference optical microscope. Yellow diamonds show the critical layer thickness reported by Hearne et al. (b) Crack density as a function of layer thickness. (For interpretation of the references to colour in this figure legend, the reader is referred to the Web version of this article.)

results of 10.1 %.

During the MOCVD epitaxy of AlGaN, carbon, hydrogen, and oxygen originated from metalorganic precursors, carrier gases, and residual water vapor in the chamber. Carbon and oxygen impurities can occupy nitrogen sites in AlGaN to form substitutional defects (C_N and O_N). Moreover, the introduction of C_N and O_N significantly reduces the formation energy of nearby nitrogen vacancies (V_N) [28]. These defects introduce deep-level trap states [29] in the band structure, thereby affecting the observation of bandgap properties (exciton transition energies) via PL and reflectance spectroscopy. Accordingly, the impurity analysis was conducted. The observable C and O signal in Fig. 2(a) indicates the presence of C and O impurities, in agreement with TEM/EDX results. Overall, the slight C 1s and O 1s peak indicates a low level of carbon and oxygen content, consistent with our previous SIMS measurements that carbon and oxygen are evenly distributed along the growth direction and both have low concentrations of 10^{16} cm^{-3} [30]. This is mainly because these contents are related to growth temperature and precursor flow rate, but is nearly independent of growth pressure in MOCVD growth. Higher growth temperatures promote more complete decomposition of TMA and TMG, avoiding the incorporation of organic groups into films. Additionally, compared to Ga–C bonds, Al–C bonds exhibit a stronger affinity [31]; therefore, carbon content remains minimal for low Al compositions. As shown in Fig. 2(e and f), Gaussian deconvolution of the O 1s and C 1s core-level spectra reveals that the O 1s spectrum contains a dominant C-O/O-C=O at 534.1 eV and Al-O at 530.0 eV [32]. The core-level C 1s peak can be divided into three subpeaks ascribed to C-C/C-H (287.0 eV), C-O (287.8 eV), and O-C=O (291.0 eV) [33]. The two high-energy shoulder peaks observed in the C 1s spectrum correspond well with the O 1s peak, indicating possible incorporation of carbon/oxygen during the growth process from precursors in the sample. It should be noted that due to hydrogen containing only one electron, XPS is insensitive to H and cannot directly detect hydrogen impurities. Then, the possible pathway for hydrogen impurities is methyl groups ($–CH_3$) from the decomposition of precursors (TMA and/or TMI) or from residual water vapor incorporated during growth in the MOCVD growth environment. However, high growth temperatures make the complete decomposition of precursors and a stronger affinity of Al-C result in minimal carbon content, which

also limits the hydrogen content. On the other hand, the epitaxial growth temperature of 960 °C for AlGaN films is much higher than the thermal decomposition temperature of H_2O and related species, and this very high ambient temperature leads to increased decomposition of water impinging on the surface. Furthermore, the high total gas flow rate of 72 slm prevents residual water from having sufficient surface residence time, leading to rapid desorption. It is concluded that the AlGaN samples grown in this study likely contain only minor carbon and oxygen impurities and negligible contents of hydrogen.

3.2. Critical layer thickness of AlGaN

The critical layer thickness, $h_{crit}(x)$, of AlGaN single layers grown on 4.5 μm thick GaN on sapphire was first investigated by observing the onset of cracking with increasing AlGaN thickness $h(x)$ for various x. The $Al_xGa_{1-x}N$ thickness is plotted against x in Fig. 3(a), distinguishing samples above (black solid triangles) and below (red solid circles) the critical layer thickness. The thickness above the critical layer thickness implies that cracking was observed on the sample surface, and the onset thickness of cracking corresponds to the experimental critical layer thickness. Also shown by the yellow diamonds are the reported $h_{crit}(x)$ of Hearne et al. determined by the in-situ curvature monitoring during growth [34]. It was found that the $h_{crit}(x)$ curve calculated using the following Eq. (1) proposed by Pristovsek [35] as shown by the blue curve agrees very well with our experimental results when 1.05 eV/nm^2 of E_{crit} was assumed for the energy at the onset of relaxation.

$$h_{crit}(x) = \frac{1}{2G_x}\left(\frac{1-\nu_x}{1+\nu_x}\right)\frac{E_{crit}}{f^2(x)} \quad (1)$$

where $f(x)$ is the misfit $\frac{a_x - a_0}{a_0}$, G_x the shear modulus, ν_x the Poisson ratio, with these values being calculated based on the material parameters reported by Vurgaftman and Meyer [11]. For the samples with cracks, as their thickness $h(x)$ becomes larger than the $h_{crit}(x)$, the density of cracks was confirmed to increase accordingly with increasing the amount $[h(x) - h_{crit}(x)]/h_{crit}(x)$, which is displayed by Fig. 3(b).

Eq. (1) is based on the energy balance model, where the areal strain density [36], E_H, associated with the layer thickness, $h(x)$, is given by

$$E_H = 2G_x\left(\frac{1+\nu_x}{1-\nu_x}\right)h(x)f^2(x). \quad (2)$$

The areal strain density increases proportionally to the thickness and to the square of the misfit. At the critical thickness, $h(x) = h_{crit}(x)$, the areal strain density exceeds the formation energy of dislocations, such as cracks and misfit dislocations, and lattice relaxation begins to occur, leading that Eq. (2) becomes essentially identical to Eq. (1) at the critical film thickness where the areal strain energy is equal to the formation energy of dislocations, $E_H = E_{crit}(x)$. The excellent coincidence between the curve and experiment shown in Fig. 3(a) indicates that the energy necessary for the onset of relaxation doesn't change significantly with x in this small compositional range. The E_{crit} value of 1.05 eV/nm^2 determined here for AlGaN appears significantly smaller than the 4.6 eV/nm^2 of $In_yGa_{1-y}N$ [37–40] evaluated using the same source of material parameters (not shown here). Contrary to the compressively strained InGaN of which the relaxation mechanism is mainly the formation of misfit dislocations near the hetero-interface [41], the AlGaN has tensile strain and can relax through cracking and the formation of misfit dislocations. However, for (0001)-oriented nitrides films, effective slip systems for misfit dislocations near the hetero-interface are not readily available [34]. This is the reason why E_{crit} in the InGaN/GaN system becomes so large. While in the AlGaN/GaN system, the initial relaxation is due to the formation and propagation of cracks, which in turn activates slip systems for misfit dislocation [34]. Therefore, finding just cracking lines on the surface is enough to look for the onset of relaxation. The following studies are carried out using the samples chosen among the red solid circles in Fig. 3(a).

3.3. Determination of the strain states of $Al_xGa_{1-x}N$ films and GaN underlayer

When AlGaN layers are grown on sufficiently thick GaN layers like on bulk GaN substrates, the strain states of AlGaN can be readily determined by assuming that the lattice of AlGaN in the a-direction is aligned to that of unstrained GaN and only AlGaN layers are fully strained. In this case, the misfit, in-plane biaxial strain of $Al_xGa_{1-x}N$ ($\epsilon_{xx} = \epsilon_{yy}$) is $\frac{a_{GaN} - a_{AlGaN}(x)}{a_{AlGaN}(x)}$, and the out-of-plane strain (ϵ_{zz}) in the c-direction in AlGaN of hexagonal structure can be calculated simply using the stiffness coefficients of $Al_xGa_{1-x}N$ as $-2\frac{C_{13}(x)}{C_{33}(x)}\epsilon_{xx}$. Here, $a_{AlGaN}(x)$, can be calculated by linearly interpolating a_{GaN} and a_{AlN} of free-standing values at x (Vegard's law), and c_{i3}(i = 1, 3) is also determined by interpolation between c_{i3}(GaN) and c_{i3}(AlN). Since the lattice in the a-direction matches to that of GaN in the pseudomorphic hexagonal planar films grown on the c-plane and its strain can be measured conveniently in the c-direction by XRD, the mismatch strain $\epsilon_{zz} = \frac{c_{GaN} - c_{AlGaN}(x)}{c_{AlGaN}(x)}$ is used instead of $\frac{a_{GaN} - a_{AlGaN}(x)}{a_{AlGaN}(x)}$, and the positive mismatch in ϵ_{xx} means that the pseudomorphic AlGaN layer has a tensile strain resulting in a negative ϵ_{zz} strain of AlGaN in the c-direction, a shrunk lattice spacing in the c-direction compared to the unstrained lattice. These behaviors are illustrated in Fig. 4 by the blue broken lines.

However, when the AlGaN layers are grown on GaN/sapphire templates, the GaN layers, typically several micrometers thick, will receive both influences from the bottom sapphire and top AlGaN, changing their strain states. The influence of sapphire arises from the difference in the thermal expansion coefficients between sapphire and GaN. If the GaN thickness is smaller than 4 μm, the out-of-plane strain $\Delta c/c_0$ of GaN amounts as large as $1.1–1.2 \times 10^{-3}$ (the lattice constant of GaN in the c-direction is expanded from 5.185 to more than 5.190 Å) [41]. But this strain of GaN can be relaxed as the thickness of GaN, d_{GaN}, increases further, by forming micro-cracks near the sapphire/GaN interface, approaching to the free-standing value of 5.1850 Å when d_{GaN} becomes larger than 70 μm, as Hiramatsu et al. reported in detail [41]. They showed the fitting curve $c_{GaN}^{sap}(d_{GaN})$, which represents how the c-lattice constant of GaN grown on sapphire substrate changes depending on the thickness of GaN as is shown by the black curve in Fig. 5(a) and is used in the following model calculation. Owing to the low Al composition and small thickness of the AlGaN epitaxial layer in this work, the overall

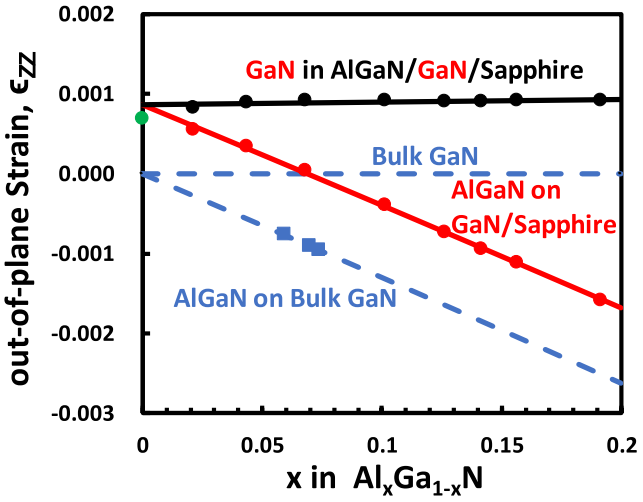

Fig. 4. The calculated strain of each layer in the structure; Red circles indicate the strain of the studied AlGaN layer grown on GaN/sapphire templates, plotted against x. The black circles are the strain of GaN layers sandwiched by sapphire and AlGaN. The blue lines and rectangles show the case when AlGaN layers are grown on bulk GaN substrates. (For interpretation of the references to colour in this figure legend, the reader is referred to the Web version of this article.)

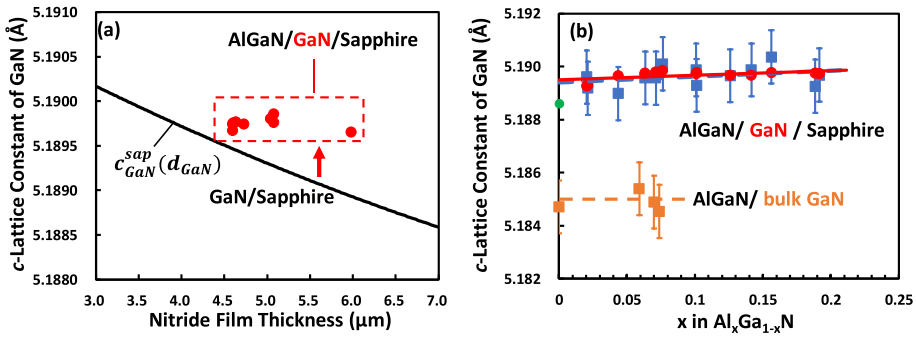

Fig. 5. (a) The change in the *c*-lattice constant of GaN grown on sapphire depending on the nitride film thickness. The black curve shows how the *c*-lattice constant relaxes as increasing the GaN thickness grown on sapphire. (b) The red solid circles show the calculated *c*-lattice constants of GaN sandwiched by sapphire and AlGaN depending on the total film thickness of GaN and AlGaN. The calculated (red solid circles) and measured (blue solid rectangles with error bars) values of the *c*-lattice constant of GaN in the AlGaN/GaN/sapphire structure plotted versus Al content. The red solid line and blue broken line are the trend lines of the calculated and measured data, respectively. (For interpretation of the references to colour in this figure legend, the reader is referred to the Web version of this article.)

amount of AlN becomes less than 1 % in the whole nitrides, thus the GaN thickness can be reasonably replaced by the total thickness of GaN and AlGaN, $d_{\mathrm{total}} = d_{\mathrm{GaN}} + d_{\mathrm{AlGaN}}$.

On the other hand, the actual strain of GaN due to the top AlGaN is determined by the balance of opposite misfit strains between GaN and AlGaN and can be calculated by multiplying their thickness ratio by $(\Delta c/c)_{\mathrm{GaN}}^{max}(x) = -2\frac{c_{13}(\mathrm{GaN})}{c_{33}(\mathrm{GaN})} \times \left(a_{\mathrm{Al}_x\mathrm{Ga}_{1-x}\mathrm{N}}(x) - a_{\mathrm{GaN}}\right)/a_{\mathrm{GaN}}$, which stands for the maximum strain of GaN assuming its lattice in *a*-direction is virtually aligned to that of a thick free-standing $Al_xGa_{1-x}N$. Because the lattice constant of AlGaN is smaller than that of GaN, the GaN layer is compressively strained, having the same sign of strain as the effect of sapphire, as indicated by an arrow in Fig. 5(a). Thus, the *c*-lattice constant of GaN, c_{GaN}, can be expressed by Eq. (3). The calculated c_{GaN} are shown by the red solid circles in Fig. 5(a) as a function of d_{total}, and in Fig. 5(b) as a function of *x* in the $Al_xGa_{1-x}N$ layers.

$$c_{GaN} = c_{\mathrm{GaN}}^{\mathrm{sap}}(d_{\mathrm{total}}) \times \left\{1 + \left[(\Delta c/c)_{\mathrm{GaN}}^{max}(x) \times \frac{d_{\mathrm{Al}_x\mathrm{Ga}_{1-x}\mathrm{N}}}{d_{\mathrm{total}}}\right]\right\} \tag{3}$$

in order to ensure the availability of this equation, the absolute value of the *c*-lattice constant of the strained GaN layers of the samples was measured using the two-plane method by XRD [15]. This method is used to improve the measurement accuracy of the absolute *c*-lattice constant, based on the following equation.

$$c = d_{(0001)} = \frac{2\lambda}{2\sin(\theta_{(0002)} + \alpha)} = \frac{4\lambda}{2\sin(\theta_{(0004)} + \alpha)}, \tag{4}$$

with which the accuracy in *c*-lattice constant can be improved. By measuring the two reflection angles θ on (0002) and (0004) planes, the value of error angle α can be deduced, and thereby more accurate *c*-constant can be determined. λ is the wavelength of the X-ray, 1.54056 Å. And the measured c_{GaN} are shown by blue solid rectangles with error bars in Fig. 5(b). Even with the two-plane method, the measured values were scattering considerably within a remaining error range of $\sim \pm$ 0.0007 Å. These measured values are compared with the calculated ones from Eq. (3) using the trend lines shown by the red solid line (calculated) and the blue broken line (measured), showing very good agreement with each other. Thus, the availability of Eq. (3) is established. And the *c*-lattice constant of GaN in the AlGaN/GaN/sapphire stays almost constant as can be seen in Fig. 5(b), because the thickness of AlGaN becomes smaller with increasing *x* in our samples, as shown in Fig. 3.

These c_{GaN} mean that the GaN layers in the samples have a smaller *a*-lattice constant than the free-standing value, to which the top AlGaN layers should align, implying that similar positive out-of-plane strains, $\Delta c/c(AlGaN)$, must be added also to the strain in AlGaN layers shown by the blue broken curve in Fig. 4. Here the strain of GaN, $\Delta c/c$ can be calculated using the above-strained value, c_{GaN}^{str} and the unstrained c_{GaN}^{0} by $\Delta c/c(\mathrm{GaN}) = \frac{\left(c_{GaN}^{str} - c_{GaN}^{0}\right)}{c_{GaN}^{0}}$, which is shown by the black filling circles in Fig. 4 and the black curve is drawn using the red trend line in Fig. 5(b). According to the balance opposite in-plane strain, i.e. $|\epsilon_{xx}(AlGaN)| = |\epsilon_{xx}(GaN)|$, the strain of AlGaN grown on the templates, $\Delta c/c(AlGaN)$ can be calculated by multiplying a stiffness factor $f_s = \frac{c_{13}(\mathrm{AlGaN})}{c_{33}(\mathrm{AlGaN})} \times \frac{c_{33}(\mathrm{GaN})}{c_{13}(\mathrm{GaN})}$ to $\Delta c/c(\mathrm{GaN})$, although this factor is very close to unity ($1 < f_s < 1.016$). The resulting strain states of AlGaN are shown by the red solid circles in Fig. 4 and the red solid curve is drawn also using the trend line in Fig. 5 (b). It should be noted here that the GaN sample has a structure with a thin InGaN layer, which is different from the structure of AlGaN

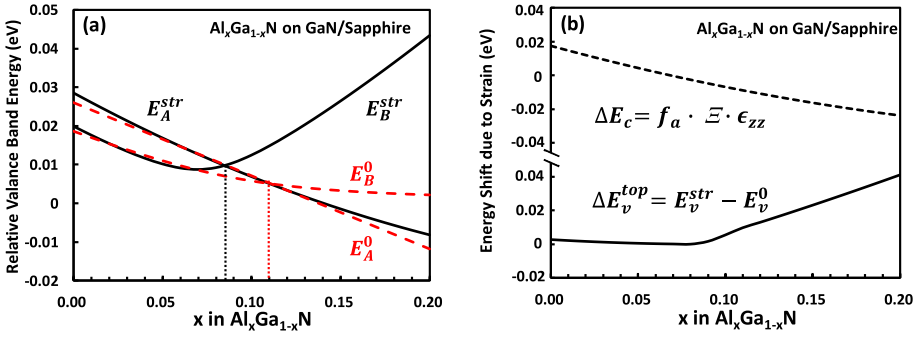

Fig. 6. (a) The calculated relative valence band energies as functions of Al-composition. Black solid curves show the change of valence band energies under a particular strain of AlGaN grown on GaN/sapphire as shown in Fig. 4. Red broken curves show the change of valence band energies for strain-free AlGaN. (b) Calculated energy shift of the top valence band (solid curve) and conduction band (broken curve) as functions of Al-composition. (For interpretation of the references to colour in this figure legend, the reader is referred to the Web version of this article.)

samples, and the data point of GaN ($x = 0$) which is shown by the green circle in Fig. 4 is not on the red solid curve of AlGaN.

3.4. Strain shift of bandgap energy

The change of relative valence band energies at Γ point as a function of x at specific out-of-plane biaxial strain, $\varepsilon_{zz}(x)$, for the A-band (Γ_9^v), $E_A^{str}(x)$ and for the B-band (upper Γ_7^v), $E_B^{str}(x)$ are given by the following equations on the basis of cubic approximation [16].

$$E_A^{str}(x) = \Delta_1(x) + \Delta_2(x) + \left[\left(D_1(x) - \frac{C_{33}(x)}{C_{13}(x)}D_2(x)\right) + \left(D_3(x) - \frac{C_{33}(x)}{C_{13}(x)}D_4(x)\right)\right]\epsilon_{zz}(x) \quad (5)$$

$$E_B^{str}(x) = \frac{\Delta_1(x) - \Delta_2(x) + \left(D_3(x) - \frac{C_{33}(x)}{C_{13}(x)}D_4(x)\right)\epsilon_{zz}(x)}{2} + \left(D_1(x) - \frac{C_{33}(x)}{C_{13}(x)}D_2(x)\right)\epsilon_{zz}(x) + \sqrt{\left(\frac{\Delta_1(x) - \Delta_2(x) + \left(D_3(x) - \frac{C_{33}(x)}{C_{13}(x)}D_4(x)\right)\epsilon_{zz}(x)}{2}\right)^2 + (2\Delta_2(x))^2}, \quad (6)$$

where Δ_1 is the crystal field splitting, $3\Delta_2$ is the spin-orbit splitting, D_i $(i = 1-4)$ are the deformation potential constants and c_{ij} are the elastic stiffness constants. All these quantities are calculated by linear interpolation between GaN ($x = 0$) and AlN ($x = 1$) and the band parameters of the end binaries were also taken from Ref. 11. The red solid curve in Fig. 4 was used for $\epsilon_{zz}(x)$. The unstrained energies, E_A^0 and E_B^0 can be calculated by setting $\epsilon_{zz}(x) = 0$ in Eqs. (5) and (6). Fig. 6(a) represents the calculated results of the relative A- and B-valence band energies for the strain-free $Al_xGa_{1-x}N$ (red broken lines) and the strained $Al_xGa_{1-x}N$ on the GaN/sapphire templates (black solid lines). The energy shift of the top valence band due to strain, $\Delta E_v^{top} = E_v^{str} - E_v^0$ then becomes $E_A^{str} - E_A^0$ for $0 \le x < 0.085$, $E_B^{str} - E_A^0$ for $0.085 \le x < 0.11$, and $E_B^{str} - E_B^0$ for $0.11 \le x$. This is the reason why the slope of the calculated curve of ΔE_v^{top} changes suddenly at x of 0.085 and 0.11, as shown by the black solid curve in Fig. 6(b).

In addition, the change of the conduction band energy due to biaxial strain can be calculated by the following equation.

$$\Delta E_c = \Xi \cdot \epsilon_{zz}(x) = \left[(a_1(x) + D_1(x)) - \frac{C_{33}(x)}{C_{13}(x)}(a_2(x) + D_2(x))\right] \cdot \epsilon_{zz}(x) \quad (7)$$

where Ξ is the combined dilatational component of the deformation potential acting on the conduction band, a_1 and a_2 are the hydrostatic interband deformation potentials in the z- and x,y-directions, respectively, and were also taken from Ref. 11. However, since these parameters include some uncertainty, as pointed out in the Ref. 11, an adjusting factor $f_a = 1.087$ is multiplied to Eq. (7) in order to maintain the consistency with the experiment [16], so that the slope of A-exciton with respect to ϵ_{zz}; $\Xi - \left[\left(D_1 - \frac{C_{33}}{C_{13}}D_2\right) + \left(D_3 - \frac{C_{33}}{C_{13}}D_4\right)\right]$ can take the same figure with the experimental 15.4 eV of GaN. Thus, the calculated ΔE_c is shown by the black broken curve in Fig. 6(b).

The calculation of the strain shift in the bandgap energies, ΔE_g for the AlGaN layers grown on GaN/sapphire templates is then finalized by calculating $\Delta E_c - \Delta E_v^{top}$ using the curves in Fig. 6(b) and is shown in Fig. 7 as a function of x, together with the case of the AlGaN layers grown on bulk GaN substrates. The data calculated for the employed samples in the following measurements are shown by the red solid circles and blue rectangles for AlGaN on GaN/sapphire and bulk GaN, respectively.

3.5. Measurements of the bandgap energies for strained AlGaN layers

The temperature evolution of the PL spectra is utilized to analyse the excitonic transition in the $Al_xGa_{1-x}N$ ($0 \le x < 0.2$) epilayer. To obtain the exact exciton transition energy, a low excitation energy of 0.03 μJ (29.8 kW/cm^2) was used during the PL measurements to avoid some nonlinear processes like the exciton-exciton scattering and biexcitons, and the band-filling effect. Additionally, in order to eliminate the influence of the Burstein-Moss effect, which causes the optical bandgap to shift higher energy when the electron concentration of the material exceeds

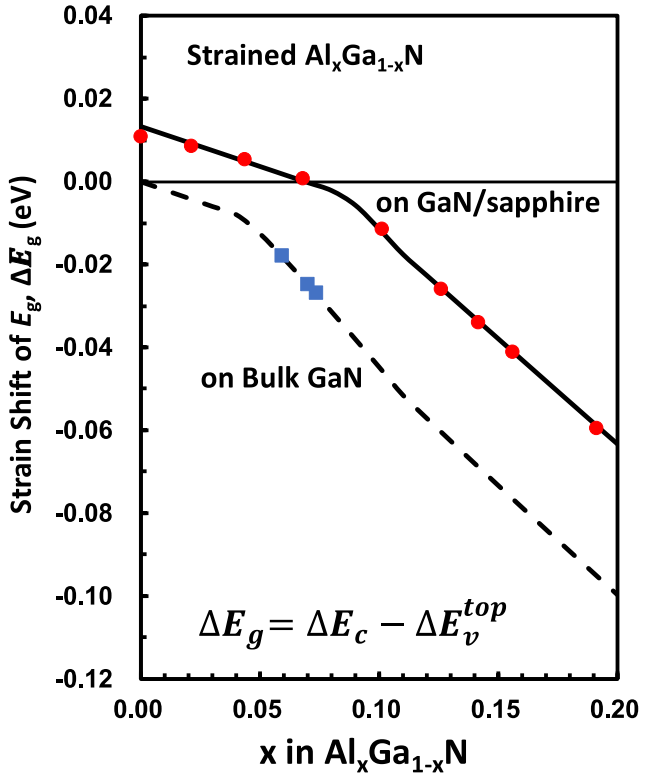

Fig. 7. Calculated shift in the bandgap energy due to strain, ΔE_g of $Al_xGa_{1-x}N$ grown on GaN/sapphire and bulk GaN. Curves are drawn using the strain curves shown in Fig. 4. The red solid circles and blue solid rectangles are the calculated shifts for the samples employed. (For interpretation of the references to colour in this figure legend, the reader is referred to the Web version of this article.)

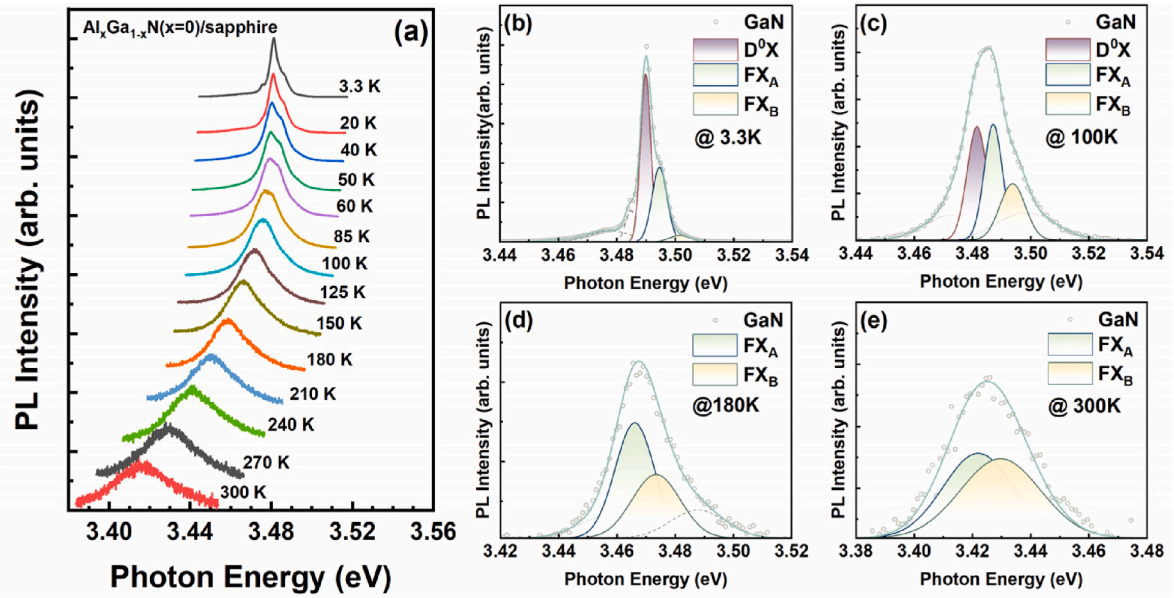

Fig. 8. (a) Temperature-dependent PL spectra for an $Al_xGa_{1-x}N$ ($x = 0$, i.e. GaN) epilayer across a temperature range from 3.3 K to 300 K. The PL spectra measured at (b) 3.3 K, (c) 100 K, (d) 180 K, and (e) 300 K, along with the numerically deconvoluted results using Gaussian fitting, showing the peak positions of the bound exciton and the free excitons A and B.

the degeneracy limit of 10^{18} cm^{-3} for III-nitride semiconductors [42], all samples were intentionally undoped and the background electron density of the $Al_xGa_{1-x}N$ ($x = 0$, i.e. GaN) epitaxial layers was estimated to be approximately 10^{15} cm^{-3} in this work.

Fig. 8(a) shows normalized temperature-dependent PL (TDPL) spectra for the $Al_xGa_{1-x}N$ ($x = 0$, i.e., GaN) layers for a temperature range from 3.3 to 300 K. The TDPL spectra are numerically deconvoluted, using as few Gaussian peaks as possible because the energy separation between A-band and B-band is as small as 8 meV and the apparent thermal broadening of PL peak with increasing temperature. At 3.3K, as shown in Fig. 8(b), the PL peak is usually dominated by the bound exciton. Then the three interesting emission lines at 3.489, 3.495, and 3.503 eV are assigned to the recombination of the neutral donor bound exciton (D^0X), the free exciton of A- (FX_A), and B- (FX_B), in close agreement with those reported by Zhang et al. [43]. Most bound excitons will dissociate into free excitons due to thermal energy, thus the relative intensity of bound excitons compared to FX_A (or FX_B) decreases with increasing temperature [Fig. 8(c)]. As the temperature further increases, the bound exciton peak disappears [Fig. 8(d)], and the broadened PL peak for GaN film at room temperature ultimately represents the envelope of FX_A and FX_B emission [Fig. 8(e)].

Given the differing effective masses of heavy and light holes, the PL emission lines associated with A- and B-free excitons show very clear temperature-dependent behaviors. Fig. 9 summaries the free exciton transition energy obtained from the peak deconvolution as a function of temperature and the solid and dotted line shows the result of the fit to the experimental data using the Varshni function:

$$E_g(T) = E_g(0) - \frac{\alpha T^2}{(\beta + T)} \tag{8}$$

where $E_g(T)$ and $E_g(0)$ are the transition energy of the excitons at temperature T and 0 K, and α and β are the Varshni characteristic coefficients.

Based on the fitting, the Varshni coefficients for FX_A and FX_B were determined as $\alpha = 0.88$ meV/K, $\beta = 782.5$ K and $\alpha = 1.3$ meV/K, $\beta = 1274.3$ K, respectively. These results are in good agreement with those reported by Shan et al. [44] ($\alpha = 0.83$ meV/K, $\beta = 835.6$ K for FX_A and $\alpha = 1.1$ meV/K, $\beta = 1194.7$ K for FX_B). Thus, the above deconvolution results and subsequent assignment of free excitons are reasonable.

For the temperature-dependent PL spectra of $Al_xGa_{1-x}N$ ($0 < x < 0.2$), alloy disorder broadening prevents the observation of fine PL emission lines, such as those of GaN in Fig. 8, the typical representatives TDPL spectra of AlGaN films are shown in Fig. 10. With the increase in temperature from 3.3 K to 60 K, an initial increase in PL peak energy was observed, reflecting the thermal repopulation of excitons from localized to extended states. Along with this, the spectral shape changes from an asymmetric shape with a low energy tail to a Boltzmann-like shape with increasing temperature, as shown in Fig. 10(b) and (c), indicated that the spectrum primarily is dominated by radiative recombination of bound excitons localized at potential minima at relatively low temperature. As the temperature increases from 60 K further to room temperature, the PL peak broadens at its high-energy side [Fig. 10(d)], which is caused by the thermal excitation into higher energy levels (Maxwell-Boltzmann distribution). At the same time, the PL peak energy gradually

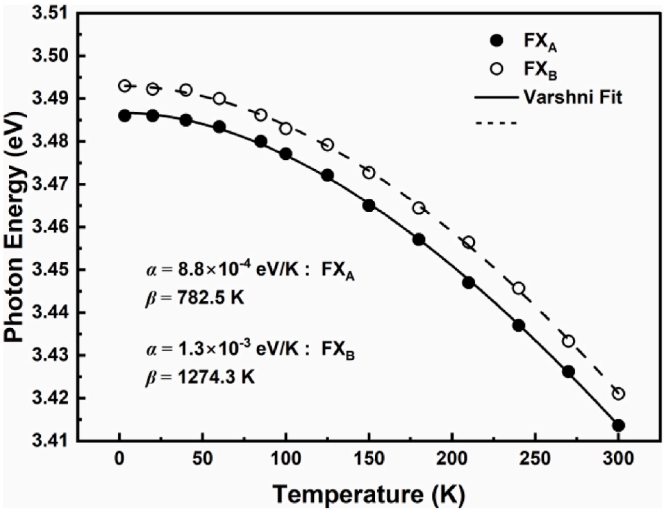

Fig. 9. The temperature dependence of photon energy for FX_A (solid circle) and FX_B (open circle) was obtained through numerical deconvolution. The solid and dotted lines represent the fits for FX_A and FX_B, respectively, using the Varshni function.

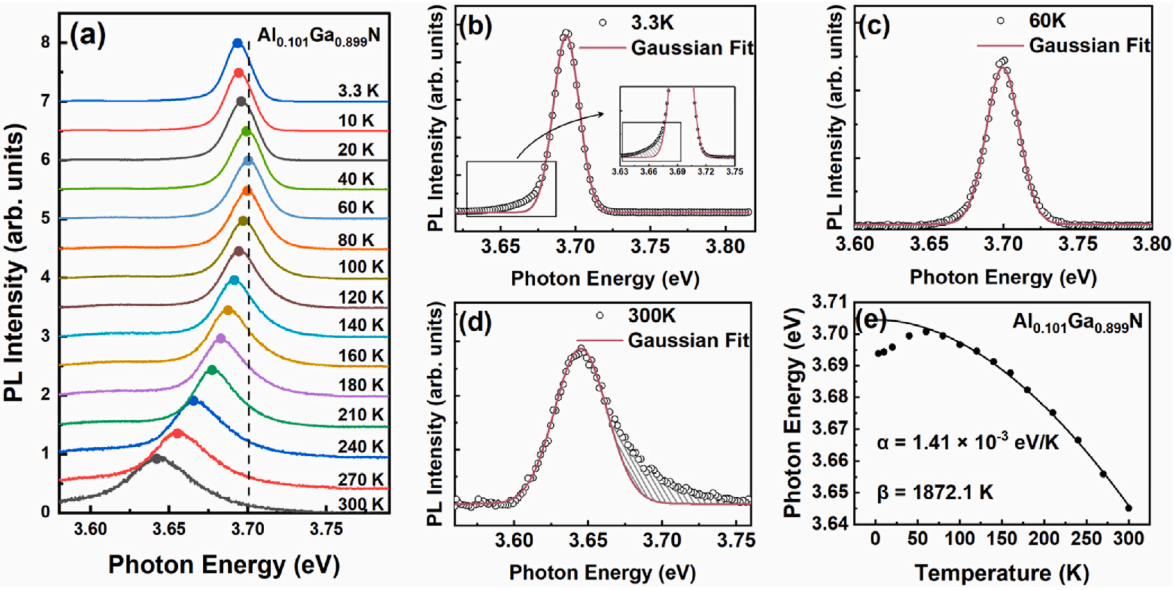

Fig. 10. (a) Temperature-dependent PL spectra for an $Al_{0.101}Ga_{0.899}N$ epilayer, with the closed circles marking the PL spectral peaks. The measured PL spectra and the corresponding Gaussian-fitted peaks at (b) 3.3 K, (c) 60 K, and (d) 300 K. (e) Temperature dependence of PL peak position for $Al_{0.101}Ga_{0.899}N$ and the solid curves are fitted Varshni function.

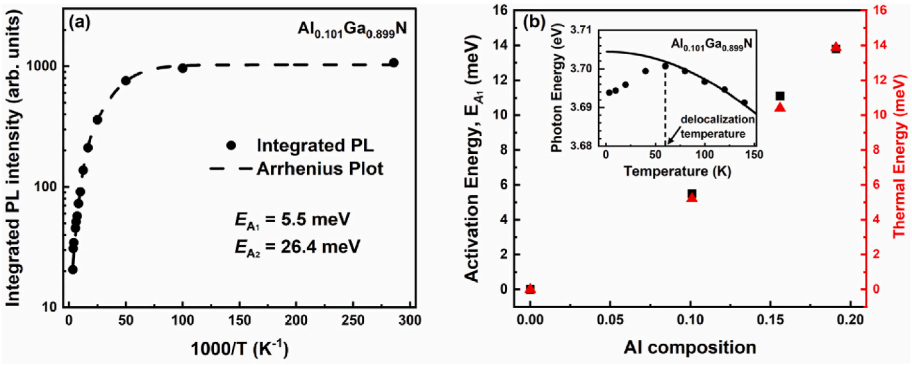

Fig. 11. (a) The Arrhenius plot of integrated PL intensity for an $Al_{0.101}Ga_{0.899}N$ epilayer, with the dashed line representing the fit obtained using Eq. (9). (b)The comparison between the activation energy of E_{A1} derived from the Arrhenius plot and the thermal energy defined by delocalization temperature. The inset shows the temperature dependence of the PL peak energy for the $Al_{0.101}Ga_{0.899}N$ epilayer, and the solid line represents the Varshni-fitted line.

shifts towards the lower energy side due to the temperature-induced shrinkage of the band-edge. This behavior can be well described by the Varshni function, as shown in Fig. 10(e). These indicate that excitons have delocalized from potential minima, leading to the radiative recombination of free excitons up to room temperature.

As shown in Fig. 11(a), it is further found that the integrated PL intensities at various temperatures can only be reproduced by the two-item Arrhenius plot, as follows:

$$I(T) = \frac{I(0)}{\left[1 + C_1 \exp\left(-\frac{E_{A_1}}{k_B T}\right) + C_2 \exp\left(-\frac{E_{A_2}}{k_B T}\right)\right]} \tag{9}$$

where $I(0)$ is the integrated PL intensity at 0 K, $C_{1,2}$ are fitting constants, and $E_{A1,2}$ are the activation energies.

To better understand the origin of the thermal quenching process and its associated activation energy, a delocalization temperature is introduced, defined as the minimum temperature within a range where the temperature dependence of the PL peak energy follows the Varshni function [45], as shown in the inset of Fig. 11(b). The delocalization temperatures are estimated to be 60, 120, and 160 K for $x = 0.101$, 0.156, and 0.191, respectively. The corresponding thermal energies at these delocalization temperatures are 5.2, 10.4, and 13.9 meV, comparable to the activation energy E_{A1}, as shown in Fig. 11(b). Therefore, the thermal quenching process, characterized by E_{A1}, is attributed to the delocalization of excitons, confirming the assignment of PL peak presented in Fig. 10. Additionally, the activation energy, E_{A2} is larger than the localization energies (E_{A1}), and it is associated with the exciton decomposition. Therefore, the value of E_{A2} corresponds to the binding energy of excitons, which is also close to the discussion of Fig. 14.

In summary, the TDPL spectra of $Al_xGa_{1-x}N$ ($0 \leq x < 0.2$) films can distinguish both bound- and free-exciton emissions at low temperatures and free-exciton emissions at high temperatures up to room temperature. It remains to be discussed whether the PL at room temperature originates from A- and/or B- free excitons, as will be further elaborated later.

For selected examples of the strained $Al_xGa_{1-x}N$ samples with various x from 0 to 0.192, the measured reflectance spectra along with the corresponding PL spectra at room temperature are plotted in Fig. 12. Note that the structures appearing in the 3.85–3.89 eV photon energy region [see Fig. 12(f)–(h)], where the source of measuring light changes from deuterium to tungsten lamps, are attributed to artifacts. At the low-energy region of the PL peak, the energy period of interference

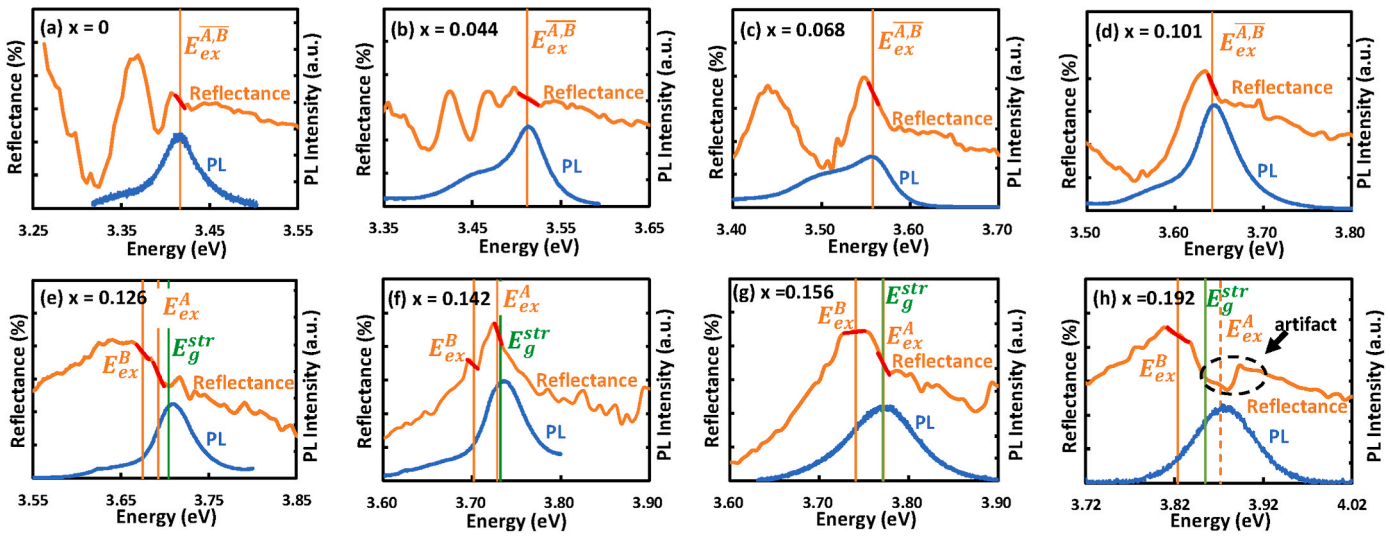

Fig. 12. Comparisons between reflectance and PL spectra, for some selected $Al_xGa_{1-x}N$ samples with (a) $x = 0$, (b) $x = 0.044$, (c) $x = 0.068$, (d) $x = 0.101$, (e) $x = 0.126$, (f) $x = 0.142$, (g) $x = 0.156$, and (h) $x = 0.192$. $E_{ex}^{\overline{AB}}$, $E_{\mathrm{ex}}^{\mathrm{A}}$, and $E_{\mathrm{ex}}^{\mathrm{B}}$ represent respectively the intermediate transition energy of A- and B- free excitons, the excitonic transition energy of FX_A, and FX_B. These are determined by the central spectral lineshape observed in the reflectance spectra and compared with the PL spectra. It should be noted that the position of $E_{\mathrm{ex}}^{\mathrm{A}}$ in Fig. 12(h) is derived from the observed $E_{\mathrm{ex}}^{\mathrm{B}}$, with the separation between them calculated from Fig. 6(a). The derived $E_{\mathrm{ex}}^{\mathrm{A}}$ also aligns with the PL peak. E_g^{str} is the band-edge energy of B-band, which equals exciton transition energy ($E_{\mathrm{ex}}^{\mathrm{B}}$) plus exciton binding energy.

oscillation becomes larger with increasing x in reflectance spectra, mainly because of the thinner AlGaN thickness as shown in Fig. 3. While, in the energy region above the PL peak, the reflectivity monotonically decreases due to above-band absorption. Importantly, a characteristic spectral lineshape, as marked by the red line in Fig. 12, can be observed in the reflectance spectra at the photon energy of PL peak originating from the free exciton except at the 19.2 % Al composition, where the reflectance spectrum cannot be accurately observed due to artifacts. This characteristic spectral lineshape, which aligns with the PL peak of the free exciton, should be related to the change in dielectric constant caused by exciton transitions. As reported by Bhattacharyya et al. [46], they modeled the dielectric function contribution from the exciton using a Lorentzian oscillator, which accurately describes this characteristic spectral lineshape in the reflectance spectra and determines the excitonic transition energies. Based on this understanding, the excitonic transition energies were carefully assigned keeping in mind the relationship of valence bands shown in Fig. 6(a).

Judging from the energy separation between the A- and B- valence bands as shown in Fig. 6(a), and given the same exciton binding energy for the A- and B- excitons, then the separation between A- and B-exciton transition energies should follow the same separation between the A- and B-valence band energies. When $x < \sim 0.10$, the separation of the two excitons ΔE_{ex}^{AB} (where $\Delta E_{ex}^{AB} = \left|E_A^{str}(x) - E_B^{str}(x)\right|$) is smaller than $\sim k_BT$ ($\sim$0.026 eV at room temperature), indicating that the A- and B-excitons are not resolved in the spectra. As a result, only one feature related to exciton transition is observed in the reflectance spectra, as shown in Fig. 12(a)–(d). The PL peak energy (or the central spectral lineshape) corresponds to the intermediate transition energy of A- and B-excitons, $E_{ex}^{\overline{A,B}}$ due to unresolved A- and B-excitons, as indicated by Fig. 8(e). According the relative position of A- and B-valence band as shown in Fig. 6(a), the excitonic transition energies can be calculated as $E_{\mathrm{ex}}^{\mathrm{A}} = E_{ex}^{\overline{AB}} - \frac{1}{2}\Delta E_{ex}^{AB}$, $E_{\mathrm{ex}}^{\mathrm{B}} = E_{ex}^{\overline{AB}} + \frac{1}{2}\Delta E_{ex}^{AB}$ for $0 \le x < 0.085$ [the top most valence band is A-], and $E_{\mathrm{ex}}^{\mathrm{A}} = E_{ex}^{\overline{AB}} + \frac{1}{2}\Delta E_{ex}^{AB}$, $E_{\mathrm{ex}}^{\mathrm{B}} = E_{ex}^{\overline{AB}} - \frac{1}{2}\Delta E_{ex}^{AB}$ for $0.085 \le x < 0.10$ [the top most valence band is B-].

On the other hand, two distinct spectral lineshapes can be observed in the reflectance spectra when x is larger than $\sim$0.10, as can be seen in Fig. 12(e)–(g), meaning the A- and B-free exciton become distinguishable. The PL peak energy (or the central spectral lineshape) corresponds to the excitonic transition energy of $E_{\mathrm{ex}}^{\mathrm{A}}$.

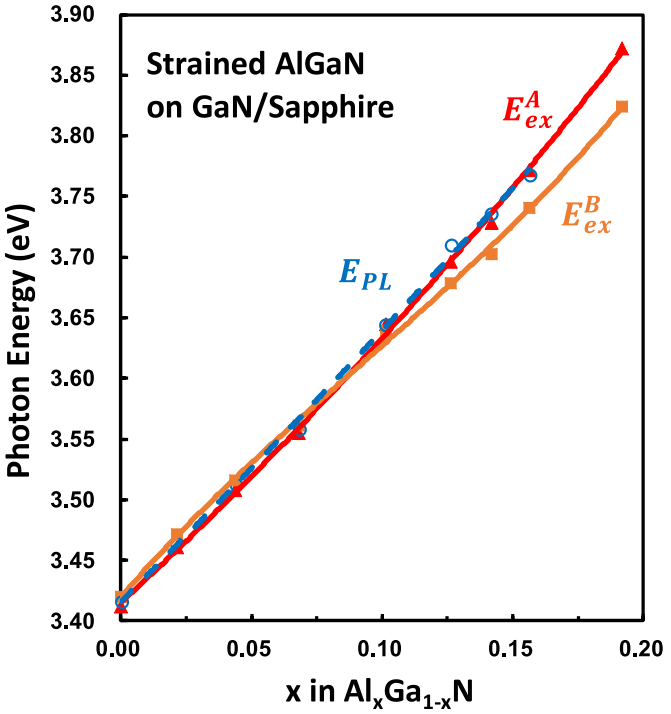

Fig. 13. The excitonic transition energies $E_{\mathrm{ex}}^{\mathrm{A}}$ and $E_{\mathrm{ex}}^{\mathrm{B}}$ determined from reflectance and the PL peak energies E_{PL} of $Al_xGa_{1-x}N$ plotted against x. The curves were drawn using 2nd order polynomial fittings for $E_{\mathrm{ex}}^{\mathrm{A}}$ and E_{PL}, and a 3rd order polynomial fitting for $E_{\mathrm{ex}}^{\mathrm{B}}$.

The determined excitonic transition energies in the reflectance are plotted against x, together with the PL peak energies, as shown in Fig. 13. As can be seen in the figures, the central excitonic energies between $E_{\mathrm{ex}}^{\mathrm{A}}$ and $E_{\mathrm{ex}}^{\mathrm{B}}$ agree very well with the PL peak energies for $0 \le x < 0.1$. In addition, this fact suggests that the Stokes shift would be negligibly small in this alloy system, contrary to InGaN. While in the

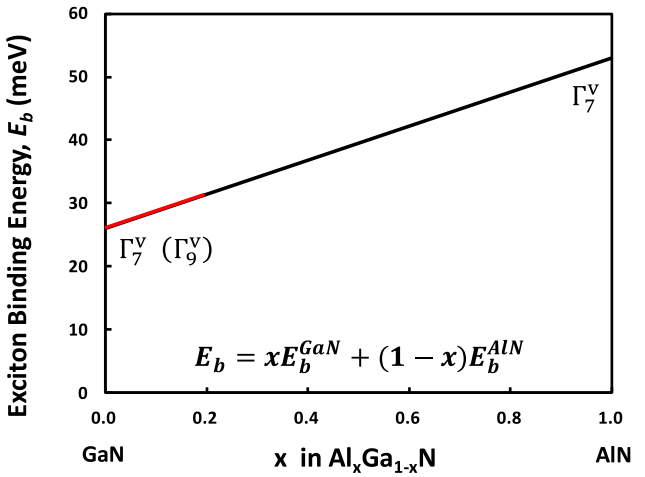

Fig. 14. The assumed linear dependence on x of exciton binding energy in $Al_xGa_{1-x}N$. The same values of E_b are taken for the different bands in GaN. The red line shows the range used in this study. (For interpretation of the references to colour in this figure legend, the reader is referred to the Web version of this article.)

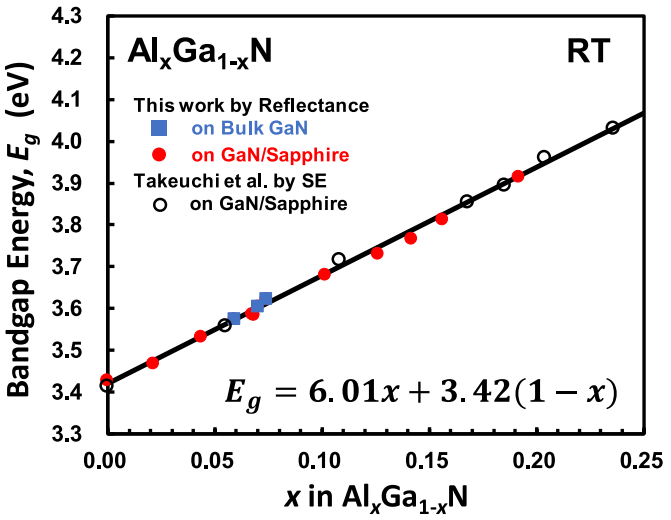

Fig. 15. The x-dependence of the strain-free bandgap energy. The red solid circles are the results of AlGaN grown on GaN/sapphire, and the blue solid rectangles are the results of AlGaN grown on bulk GaN. The black open circles were calculated by applying our method to the reported strained bandgap energies measured by spectroscopic ellipsometry by Takeuchi et al. The black line represents the linear relationship connecting two end bandgaps, between 3.42 (GaN) and 6.01 (AlN) eV. (For interpretation of the references to colour in this figure legend, the reader is referred to the Web version of this article.)

range $0.1 < x < 0.20$, the PL peak follows the E_{ex}^{A} energies rather than the energetically lower E_{ex}^{B} energies, the reason for which is that the density of states of A-valence band is essentially larger than the density of B-band, and the band-edge energy of B-band (E_g^{str}) locates energetically close to the excitonic transition energy of A-band, enhancing the PL intensity in this energy region.

From the observed lowest excitonic transition energies E_{ex}^{lowest} of strained $Al_xGa_{1-x}N$, which are E_{ex}^{A} for $0 \le x \le 0.85$, and E_{ex}^{B} for $0.85 < x$, the strain-free bandgap energy E_g can be determined if the appropriate value of exciton binding energy E_b is given, by the following equation taking into account the strain-induced band gap shift ΔE_g shown in Fig. 7.

$$E_g = E_{ex}^{lowest} + E_b - \Delta E_g. \tag{10}$$

3.6. Exciton binding energy of AlGaN

For GaN, the values of exciton binding energy E_b were reported to be 25.7 ± 0.05 meV, only weakly depending on either Γ_9^v (A) or upper Γ_7^v (B) valence bands [16,47] and on the degree of strain [34]. While for AlN, the reported E_b, which should be associated with the upper Γ_7^v valence band, ranges within 53 ± 2 meV [8–10,48]. So, the dependence of E_b on x in $Al_xGa_{1-x}N$ is simply approximated here by the linear interpolation between the two endpoints, between 26 meV (GaN) and 53 meV (AlN) similar to the other material parameters, as shown in Fig. 14.

3.7. X-dependence of bandgap energy for strain-free $Al_xGa_{1-x}N$

Now all the necessary elements to calculate the strain-free bandgap energy of AlGaN using Eq. 10 have been prepared. Using the lowest excitonic transition energy E_{ex}^{lowest} observed by reflectance and the calculated strain shift (ΔE_g) and the exciton binding energy (E_b) the calculated strain-free bandgap energies are plotted versus x in Fig. 15 by the red solid circles for the $Al_xGa_{1-x}N$ grown on GaN/sapphire and by the blue solid rectangles for $Al_xGa_{1-x}N$ grown on bulk GaN. Also plotted by the open circles are the calculated results based on the bandgap energy of strained $Al_xGa_{1-x}N$ grown on GaN/sapphire reported by Takeuchi et al. [49] They used spectroscopic ellipsometry to directly measure the bandgap, E_g^{str}. In this case, the consideration of exciton binding energy becomes unnecessary. The strain-free E_g was calculated applying our method of ΔE_g-determination described above, assuming their reported a-lattice constant of 3.182 Å for all the samples. This compressed strain due to GaN/sapphire corresponds to $\Delta c/c$ of −0.117 %, which is larger than our case because their GaN thickness (2 μm) is a bit smaller than ours (4.5 μm). At the same time, since their material parameters such as binary lattice constants and elastic stiffness coefficients are different from ours, their x were recalculated using the same parameters employed in this study [11], resulting in small increases in x by 0.004–0.009. In this way, the $E_g^{str} - \Delta E_g$ are plotted against the calibrated x in Fig. 15 (black open circles). The black line represents the linear relationship on x expressed by the following equation

$$E_g = 6.01x + 3.42(1-x) \tag{11}$$

Owing to some assumptions made and possible measurement errors, the total accuracy of E_g in this study can be roughly estimated to be around ± 0.01 eV, which nearly equals to the size of symbols in Fig. 15. All the data points are therefore consistent with this linear relationship with no bowing parameter. The coincidence of E_g for AlGaN with similar x around 0.06 but having different strain states (comparison between AlGaN grown on GaN/sapphire and bulk GaN) is also evidencing our method to determine the amount of strain shift of bandgap, ΔE_g.

A few research teams [50–52] already claimed the linear dependence of $Al_xGa_{1-x}N$ bandgap on x, but neither the strain states of AlGaN layers nor associated shifts of the bandgap were described in their articles, and the value of ~6.2 eV was taken for the AlN bandgap energy, although Ochalski et al. [52] pointed out the importance of strain effects in AlGaN layers to determine the exact bandgap energies. To further clarify the dependence for $Al_xGa_{1-x}N$ layers with higher x, the issues such as material quality and accurate material parameters of AlN, and the non-linearities of the material parameters on x if any, are needed to be addressed.

4. Conclusions

The Al-composition dependence of strain-free bandgap energy of $Al_xGa_{1-x}N$ ($0 \le x < 0.2$) at room temperature was studied taking into account all the relevant effects. The AlGaN layer thickness was kept smaller than the critical layer thickness to minimize possible

degradation issues due to defects. First, the strain states of the $Al_xGa_{1-x}N$ were determined based on the sample structures. The strain shifts of the bandgap energies were calculated theoretically using the measured strain values and material parameters taken from the literature. The lowest excitonic transition energies were then measured by reflectance and compared with photoluminescence peak energies. The exciton binding energies were approximated by a linear interpolation of GaN and AlN. The strain-free bandgap energies were finally determined by adding the exciton binding energies and subtracting the bandgap shifts due to strain to the measured lowest excitonic transition energies. The resultant strain-free bandgap energies were consistent with the linear relationship line connecting the two end binaries, within experimental errors of ±0.01 eV. The bowing parameter was concluded to be zero in $Al_xGa_{1-x}N$ ($0 \leq x < 0.2$).

CRediT authorship contribution statement

Shaosheng Fan: Writing – review & editing, Writing – original draft, Investigation, Formal analysis, Data curation. **Masao Ikeda:** Writing – review & editing, Writing – original draft, Supervision, Investigation, Formal analysis, Data curation. **Baoping Zhang:** Writing – review & editing, Writing – original draft, Supervision, Methodology, Data curation. **Siyi Huang:** Methodology, Data curation. **Yang Mei:** Writing – review & editing, Supervision. **Jianping Liu:** Methodology. **Zongliang Liu:** Funding acquisition. **Ke Xu:** Project administration.

Declaration of competing interest

The authors declare that they have no known competing financial interests or personal relationships that could have appeared to influence the work reported in this paper.

Acknowledgments

This work was supported by the Shenzhen Science and Technology Program (No. ZDSYS20220527171201003), National Natural Science Foundation of China (Nos. 62150710548, 62234011, 62104204, and U21A20493) and the National Key Research and Development Program of China (No. 2022YFB3605800 and 2022YFB3605802). The authors would like to thank Jia-Cong Guo of Xiamen University, Xu-Jun Su, Li Zhang, Miao Wang, and Rong-Kun Ji of Suzhou Institute of Nano-Tech and Nano-Bionics, Chinese Academy of Sciences for their support and useful discussions.

Appendix A. Supplementary data

Supplementary data to this article can be found online at https://doi.org/10.1016/j.vacuum.2025.114714.

Data availability

Data will be made available on request.

References

[1] M. Amirhoseiny, G. Alahyarizadeh, The effect of AlGaN bulk and AlGaN/GaN superlattice cladding layers on performance characteristics of deep violet InGaN DQW lasers, Vacuum 141 (2017) 139–143.
[2] Y. Mei, M.C. Xie, T. Yang, X. Hou, W. Ou, H. Long, L.Y. Ying, Y.J. Liu, G.E. Weng, S. Q. Chen, B.P. Zhang, Improvement of the emission intensity of GaN-Based micro-light emitting diodes by a suspended structure, ACS Photonics 9 (12) (2022) 3967–3973.
[3] A. Pandey, V.K. Singh, S. Dalal, R.K. Bag, K. Narang, D. Kaur, R. Raman, R. Tyagi, Effect of two step GaN buffer on the structural and electrical characteristics in AlGaN/GaN heterostructure, Vacuum 178 (2020) 109442.
[4] M. Kneissl, T. Kolbe, C. Chua, V. Kueller, N. Lobo, J. Stellmach, A. Knauer, H. Rodriguez, S. Einfeldt, Z. Yang, N.M. Johnson, M. Weyers, Advances in group III-nitride-based deep UV light-emitting diode technology, Semicond. Sci. Technol. 26 (2011) 014036.
[5] Z.M. Zheng, Y. Mei, H. Long, Z.W. Zheng, J. Hoo, S.P. Guo, Q.X. Li, L. Y Ying, B. P Zhang, AlGaN-Based deep ultraviolet vertical-cavity surface-emitting laser, IEEE Electron Device Lett. 42 (3) (2021) 375–378.
[6] S.R. Lee, A.F. Wright, M.H. Crawford, G.A. Petersen, J. Han, R.M. Biefeld, The band-gap bowing of $Al_xGa_{1-x}N$ alloys, Appl. Phys. Lett. 74 (22) (1999) 3344–3346.
[7] W.M. Yim, E.J. Stofko, P.J. Zanzucchi, J.I. Pankove, M. Ettenberg, S.L. Gibert, Epitaxially grown AlN and its optical band gap, J. Appl. Phys. 44 (1) (1973) 292–296.
[8] M. Feneberg, B. Neuschl, K. Thonke, R. Collazo, A. Rice, Z. Sitar, R. Dalmau, J. Xie, S. Mita, R. Goldhahn, Sharp bound and free exciton lines from homoepitaxial AlN, Phys. Status Solidi A 208 (7) (2011) 1520–1522.
[9] H. Ikeda, T. Okamura, K. Matsukawa, T. Sota, M. Sugawara, T. Hoshi, P. Cantu, R. Sharma, J.F. Kaeding, S. Keller, U. Mishra, K. Kosaka, K. Asai, S. Sumiya, T. Shibata, M. Tanaka, J.S. Speck, S.P. DenBaars, S. Nakamura, T. Koyama, T. Onuma, S. Chichibu, Impact of strain on free-exciton resonance energies in wurtzite AlN, J. Appl. Phys. 102 (12) (2007) 123707.
[10] C. Reich, M. Feneberg, V. Kueller, A. Knauer, T. Wernicke, J. Schlegel, M. Frentrup, R. Goldhahn, M. Weyers, M. Kneissl, Excitonic recombination in epitaxial lateral overgrown AlN on sapphire, Appl. Phys. Lett. 103 (21) (2013) 212108.
[11] Meyer Vurgaftman, Band parameters for nitrogen-containing semiconductors, J. Appl. Phys. 94 (6) (2003) 3675–3696.
[12] M. Feneberg, M.F. Romero, M. Röppischer, C. Cobet, N. Esser, B. Neuschl, K. Thonke, M. Bickermann, R. Goldhahn, Anisotropic absorption and emission of bulk (1-100) AlN, Phys. Rev. B 87 (23) (2013) 235209.
[13] L.T. Romano, C.G. Van de Walle, J.W. Ager III, W. Götz, R.S. Kern, Effect of Si doping on strain, cracking, and microstructure in GaN thin films grown by metalorganic chemical vapor deposition, J. Appl. Phys. 87 (11) (2000) 7745–7752.
[14] J. Wagner, H. Obloh, M. Kunzer, M. Maier, K. Köhler, B. Johs, Dielectric function spectra of GaN, AlGaN, and GaN/AlGaN heterostructures, J. Appl. Phys. 89 (5) (2001) 2779–2785.
[15] G. Feng, X.M. Shen, J.J. Zhu, B.S. Zhang, D.G. Zhao, Y.T. Wang, H. Yang, J. W. Liang, High-resolution X-ray diffraction analysis of the Bragg peak integrated intensity in highly mismatched III-N epilayers, J. Cryst. Growth 250 (3–4) (2003) 354–358.
[16] A. Shikanai, T. Azuhata, T. Sota, S. Chichibu, A. Kuramata, K. Horino, S. Nakamura, Biaxial strain dependence of exciton resonance energies in wurtzite GaN, J. Appl. Phys. 81 (1) (1997) 417–424.
[17] G. Greczynski, L. Hultman, Impact of sample storage type on adventitious carbon and native oxide growth: X-ray photoelectron spectroscopy study, Vacuum 205 (2022) 111463.
[18] G. Greczynski, L. Hultman, Self-consistent modelling of X-ray photoelectron spectra from air-exposed polycrystalline TiN thin films, Appl. Surf. Sci. 387 (2016) 294–300.
[19] G. Greczynski, L. Hultman, A step-by-step guide to perform x-ray photoelectron spectroscopy, J. Appl. Phys. 132 (2022) 011101.
[20] G. Greczynski, L. Hultman, Compromising science by ignorant instrument calibration—need to revisit half a century of published XPS data, Angew. Chem., Int. Ed. 59 (2020) 5002.
[21] G. Greczynski, L. Hultman, The same chemical state of carbon gives rise to two peaks in X-ray photoelectron spectroscopy, Sci. Rep. 11 (2021) 11195.
[22] G. Greczynski, L. Hultman, C 1s peak of adventitious carbon aligns to the vacuum level: dire consequences for material's bonding assignment by photoelectron spectroscopy, ChemPhysChem 18 (2017) 1507.
[23] G. Greczynski, L. Hultman, Reliable determination of chemical state in x-ray photoelectron spectroscopy based on sample-work-function referencing to adventitious carbon: resolving the myth of apparent constant binding energy of the C 1s peak, Appl. Surf. Sci. 451 (2018) 99.
[24] Dominika Majchrzak, et al., Detailed surface studies on the reduction of Al incorporation into AlGaN grown by molecular beam epitaxy in the Ga-droplet regime, Vacuum 202 (2022) 111168.
[25] A.N. Hattori, K. Endo, K. Hattori, H. Daimon, Surface treatments toward obtaining clean GaN (0 0 0 1) from commercial hydride vapor phase epitaxy and metal-organic chemical vapor deposition substrates in ultrahigh vacuum, Appl. Surf. Sci. 256 (2010) 4745–4756.
[26] J.Q. Guo, K. Wei, S. Zhang, X.Q. He, Y.C. Zhang, R.Z. Zhang, J.C. Wang, K.Y. Wang, S. Huang, Y.K. Zheng, X.H. Wang, X.Y. Liu, Low damage atomic layer etching technology for gate recessed fabrication, Vacuum 217 (2023) 112591.
[27] M. Alizadeh, V. Ganesh, A. Pandikumar, B.T. Goh, S. Azianty, N.M. Huang, S. A. Rahman, Photoelectrochemical behavior of AlxIn1-xN thin films grown by plasma-assisted dual source reactive evaporation, J. Alloys Compd. 670 (2016) 229–238.
[28] H. Huang, X. Yan, X. Yang, W. Yan, Z. Qi, S. Wu, Z. Shen, N. Tang, F. Xu, X. Wang, W. Ge, B. Huang, B. Shen, Identification of carbon location in p-type GaN: Synchrotron x-ray absorption spectroscopy and theory, Appl. Phys. Lett. 121 (2022) 252101.
[29] S.F. Chichibu, K. Shima, K. Kojima, S. Ishibashi, A. Uedono, Origin and dynamic properties of major intrinsic nonradiative recombination centers in wide bandgap nitride semiconductors, Proc. SPIE Gallium Nitride Materials and Devices XV (11280) (2020) 112800B.
[30] S.Y. Huang, M. Ikeda, F. Zhang, M.L. Zhang, J.J. Zhu, S.M. Zhang, J.P. Liu, Achievable hole concentration at room temperature as a function of Mg concentration for MOCVD-grown p-GaN after sufficient annealing, J. Semiconduct. 45 (8) (2024) 082501.
[31] R.B. Chung, F. Wu, R. Shivaraman, S. Keller, S.P. DenBaars, J.S. Speck, S. Nakamura, Growth study and impurity characterization of $Al_xIn_{1-x}N$ grown by

metal organic chemical vapor deposition, J. Cryst. Growth 324 (1) (2011) 163–167.
[32] R. Sohal, P. Dudek, O. Hilt, Comparative study of NH4OH and HCl etching behaviours on AlGaN surfaces, Appl. Surf. Sci. 256 (7) (2010) 2210–2214.
[33] S. Hasan, M.U. Jewel, S.G. Karakalos, M. Gaevski, I. Ahmad, Comparative spectroscopic study of aluminum nitride grown by MOCVD in H_2 and N_2 reaction environment, Coatings 12 (2022) 924.
[34] S.J. Hearne, J. Han, S.R. Lee, J.A. Floro, D.M. Follstaedt, E. Chason, I.S.T. Tsong, Brittle-ductile relaxation kinetics of strained AlGaN/GaN heterostructures, Appl. Phys. Lett. 76 (12) (2000) 1534–1536.
[35] M. Pristovsek, Wavelength limits for InGaN quantum wells on GaN, Appl. Phys. Lett. 102 (24) (2013) 242105.
[36] R. People, J.C. Bean, Calculation of critical layer thickness versus lattice mismatch for GexSi1−x/Si strained-layer heterostructures, Appl. Phys. Lett. 47 (3) (1985) 322–324.
[37] L.T. Romano, B.S. Krusor, M.D. McCluskey, D.P. Bour, Structural and optical properties of pseudomorphic $In_xGa_{1-x}N$ alloys, Appl. Phys. Lett. 73 (13) (1998) 1757–1759.
[38] C.A. Parker, J.C. Roberts, S.M. Bedair, M.J. Reed, S.X. Liu, N.A. El-Masry, Determination of the critical layer thickness in the InGaN/GaN heterostructures, Appl. Phys. Lett. 75 (18) (1999) 2776–2778.
[39] M. Iwaya, T. Yamamoto, D. Iida, Y. Kondo, M. Sowa, H. Matsubara, K. Ishihara, T. Takeuchi, S. Kamiyama, I. Akasaki, Relationship between misfit-dislocation formation and initial threading-dislocation density in GaInN/GaN heterostructures, Jpn. J. Appl. Phys. 54 (11) (2015) 115501.
[40] G. Ju, M. Tabuchi, Y. Takeda, H. Amano, Role of threading dislocations in strain relaxation during GaInN growth monitored by real-time X-ray reflectivity, Appl. Phys. Lett. 110 (26) (2017) 262105.
[41] K. Hiramatsu, T. Detchprohm, I. Akasaki, Relaxation mechanism of thermal stresses in the heterostructure of GaN grown on sapphire by vapor phase epitaxy, Jpn. J. Appl. Phys. 32 (4R) (1993) 1528.
[42] S.A. Kazazis, E. Papadomanolaki, M. Androulidaki, M. Kayambaki, E. Iliopoulos, Optical properties of InGaN thin films in the entire composition range, J. Appl. Phys. 123 (12) (2018) 125101.
[43] F. Zhang, S.J. Xu, J.Q. Ning, C.C. Zheng, D.G. Zhao, H. Yang, C.M. Che, Optical properties of light-hole excitons in GaN epilayers, J. Appl. Phys. 108 (11) (2010) 116103.
[44] W. Shan, T.J. Schmidt, X.H. Yang, S.J. Hwang, J.J. Song, Temperature dependence of interband transitions in GaN grown by metalorganic chemical vapor deposition, Appl. Phys. Lett. 66 (8) (1995) 985.
[45] H. Murotani, Y. Yamada, T. Taguchi, A. Ishibashi, Y. Kawaguchi, T. Yokogawa, Temperature dependence of localized exciton transitions in AlGaN ternary alloy epitaxial layers, J. Appl. Phys. 104 (5) (2008) 053514.
[46] J. Bhattacharyya, A. Kadir, S. Ghosh, M.R. Gokhale, A. Bhattacharya, B.M. Arora, Reflectance spectroscopy study of epitaxial GaN films at room temperature, in: IEEE 14th Int. Workshop on Phys. Semicon. Devices, Mumbai, 2007, pp. 504–506.
[47] A.V. Rodina, M. Dietrich, A. Göldner, L. Eckey, A. Hoffmann, Al L. Efros, M. Rosen, B.K. Meyer, Free excitons in wurtzite GaN, Phys. Rev. B 64 (11) (2001) 115204.
[48] R. Ishii, M. Funato, Y. Kawakami, Effects of strong electron-hole exchange and exciton–phonon interactions on the exciton binding energy of aluminum nitride, Jpn. J. Appl. Phys. 53 (9) (2014) 091001.
[49] T. Takeuchi, H. Takeuchi, S. Sota, H. Sakai, H. Amano, I. Akasaki, Optical properties of strained AlGaN and GaInN on GaN, Jpn. J. Appl. Phys. 36 (2B) (1997) L177.
[50] D.K. Wickenden, C.B. Bargeron, W.A. Bryden, J. Miragliotta, T.J. Kistenmacher, High quality self-nucleated AlxGa1-xN layers on (00.1) sapphire by low-pressure metalorganic chemical vapor deposition, Appl. Phys. Lett. 65 (16) (1994) 2024–2026.
[51] L.C. Duta, C.B. Stagarescu, J. Downes, K.E. Smith, D. Korakakis, T.D. Moustakas, J. Guo, J. Nordgren, Density of states, hybridization, and band-gap evolution in $Al_xGa_{1-x}N$ alloys, Phys. Rev. B 58 (4) (1998) 1928.
[52] T.J. Ochalski, B. Gil, P. Lefebvre, N. Grandjean, M. Leroux, J. Massies, S. Nakamura, H. Morkoç, Photoreflectance investigations of the bowing parameter in AlGaN alloys lattice-matched to GaN, Appl. Phys. Lett. 74 (22) (1999) 3353–3355.